Polymer-derived silicon oxycarbide/graphene oxide porous ceramic monoliths obtained from Pickering emulsions. Application as active electrode for Lithium-Ion batteries

Bonito A. Karamoko[ab], Sonjoy Dey[c], Shakir B. Mujib[c], Jiefeng Liu[a], Wensen Wang[a], Ji Li[d], Gurpreet Singh[c], Damien Voiry[a], Chrystelle Salameh[a], Benjamin K Yao[b], Philippe Miele[a,e]**

[a] Institut Européen des Membranes (IEM), UMR 5635, Université Montpellier, ENSCM, CNRS, Montpellier, France

[b] Laboratory of Synthesis, Industrial Processes, Environment, and Renewable Energies, Félix Houphouët-Boigny National Polytechnic Institute of Yamoussoukro, P.O. Box 1093, Yamoussoukro, Ivory

[c] Department of Mechanical and Nuclear Engineering, Kansas State University, Manhattan, KS 66506, USA

[d] College of Bioresources and Materials Engineering, Shaanxi University of Science and Technology, Xi'an, People's Republic of China

[e] Institut Universitaire de France (IUF), MESR, Paris, France

KEYWORDS: SiOC, Graphene Oxide, Pickering Emulsions, Polymer-Derived Ceramics, Batteries

ABSTRACT

The fabrication of porous ceramic materials is of great importance for various applications in energy, catalysis, filtration and refractory applications. Achieving rational design of polymer-derived ceramics (PDC) with hierarchical porosity has been made possible with the use of porous agents, direct foaming or replicates. However, these synthetic approaches often suffer from complexity and limited control over the desired porous architectures. In this study, we report an innovative method for preparing porous polymer-derived ceramic (PDC) monoliths by combining the preceramic polymer route and the Pickering emulsion method. The emulsions were prepared using a SiOC precursor and stabilized with graphene oxide nanosheets modified with hexadecylamine. The effects of formulation on the final properties of Pickering emulsions were thoroughly studied, taking into account the emulsification process, emulsification rate, concentration of modified graphene oxide (GO) and DMSO/cyclohexane ratio. As a proof of concept, we have used the monoliths obtained as electrode materials for electrochemical energy storage in Li-ion batteries (LIBs), exhibiting higher specific capacities approximately 2 times higher than the graphite anode. Among the tested electrodes, the SiOC-GO-R16 (23%, 900 °C) electrode showed the best overall performance, displaying impressive insertion and extraction capacities of approximately 2399 $mAhg^{-1}$ and 1176 $mAhg^{-1}$ at 50 mA g^{-1}, respectively, in the first cycle. At 800 mA g^{-1}, the charge capacity was 350 mAh g^{-1} after 175 consecutive cycles, accompanied by a coulombic efficiency of 88%.

Our approach offers a novel and efficient route to fabricate porous PDC monoliths with tailored properties, and superior electrochemical performance compared to traditional PDC-based in LIBs and highlights their potential for advanced energy storage applications.

1. INTRODUCTION

The growing number of applications of porous materials in highly demanding sectors such as environment, healthcare and energy, has led to growing interest in exploring new synthesis methods. Achieving large specific surface area, ideally distributed in an accessible hierarchical porosity, and providing significant surface reactivity have become a central focus. These characteristics enable the materials to exhibit large active surface for energy storage or catalysis, among other desired functionalities. Several synthetic routes have been reported in the literature involving different fundamental concepts based on the use of hard or soft templating techniques. Examples include hydrothermal synthesis, freeze-drying, direct foaming, hard and soft replication techniques and emulsion templating [1,2]. In addition to the self-organization of amphiphilic molecules, emulsions can also be used as soft templates. In the latter case, Pickering emulsions, which are stabilized by solid particles, fall into the category of soft template-assisted emulsions that require mild conditions and are relatively straightforward to realize [3]. These emulsions exhibit relatively high interfacial attachment energy and long-term stability. These characteristics make Pickering emulsions ideal candidates as models or intermediates for the design of new porous functional materials [4]. The specific principle is to use solid particles as stabilizers for the emulsion, which then serves as the matrix for the final ceramic monolith. Once the dispersed and continuous phases have been eliminated, the particles are assembled to form the ceramic scaffold, with tunable pore size and distribution. As a result, Pickering emulsion processing can be applied to the manufacture of a variety of nanocomposite materials with open or closed porosity [5]. Porous polymer-derived ceramics (PDCs) are advanced materials that have attracted growing interest in recent years due to their unique properties and potential applications in fields such as aerospace, electronics and energy [6]. Porous polymer-derived ceramics can be classified on the basis of their

chemistry, *i.e.,* the chemical composition of the precursor and the final ceramic obtained after the heat treatment for the conversion into material. Among porous ceramics, non-oxide ceramics have received particular attention in recent years due to their excellent resistance to corrosion and oxidation and their high-temperature stability. These characteristics enable applications in harsh environments. Examples of non-oxide porous ceramics include Si_3N_4,[7] which has been proposed for hydrogen generation through $NaBH_4$ hydrolysis, and other materials such as SiC,[8] SiAlCN,[9] and SiBCN prepared using a hard template approach[10,11]. The main challenge of this method lies in the sensitivity of ceramic precursors to air and moisture [10]. In this context, silicon oxycarbide (SiOC) is a promising material because it can be obtained by pyrolysis of polysiloxanes in air or in an inert atmosphere. SiOC displays good chemical and thermal stability, can be produced at relatively low cost and is easy to process. Depending on the processing temperature, which can vary from 1000° to 2000°C under inert atmosphere, the polymer can be converted into an amorphous or crystalline ceramic containing Si-C and Si-O bonds in the presence of free amorphous carbon. SiOC is known for its high-temperature stability, high resistance to corrosion and oxidation [11]. Several research efforts have been carried out to develop porous SiOC using methods such as conventional emulsions stabilized by organic surfactants [12–17]. The integration of PDCs and in particular SiOC into negative electrodes for lithium-ion batteries (LIBs) has garnered significant interest due to their specific capacity ranges from 200 - 1300 mAh g^{-1} [18–24]. The performance of LIBs crucially depends on the nature of the materials used in the electrodes, making the quest for novel materials a highly sought-after scientific and technological challenge. Combining the PDC route with the Pickering emulsion method, opens prospects to prepare new ceramic matrix materials with hierarchical porosities presenting significant advantages for LIBs due to their large surface area and reactivity. Porous materials used as negative electrode materials

have been reported to perform better in high-speed regimes due to better penetration of the electrolyte into the deep pores. That decreases the diffusion distance of Li^+-ions during the insertion/extraction process, thus facilitating the rapid storage of Li^+-ions [25]. Two-dimensional (2D) materials such as GO [26], exfoliated smectic clay [27], boron nitride (h-BN) [28] or Mxenes [29] have been used as stabilizers for Pickering emulsions. GO is one of the most studied 2D materials, attracting attention due to its ability to bind various compounds such as amines [30] for example *via* its carbonyl, epoxy, hydroxyl, and carboxylic functional groups present on the surface. Due to their amphiphilic nature, GO nanosheets can assemble and form 3D structures at the liquid-liquid interface, for example between water and oil. Indeed, hydrophilic and hydrophobic interactions between GO sheets and the two liquids enable favorable alignment and organization at the interface. These three dimensional (3D) structures exhibit unique properties, such as porosity, conductivity and mechanical strength, and pave the way to prepare composite materials for a variety of applications [31].

In this paper, we report, for the first time, on the preparation of a porous SiOC/graphene nanocomposite material with hierarchical porosity by a combination of Pickering emulsions and the polymer-derived ceramics route. The emulsion is stabilized by hexadecylamine modified GO nanosheets as a soft template to generate porosity and the water-sensitive methyl polysiloxane precursor of SiOC is dissolved in the continuous phase. This synthesis approach allows the synthesis of porous conducting SiOC/graphene nanocomposite named SiOC-GO-R16 [X, T(°C)], Ni/SiOC-GO-R16 [X, T(°C)], where X represents the mass ratio of modified GO and T(°C) refers to the pyrolysis temperature with respect to varying amounts of preceramic polymer. We have examined the properties of the SiOC/graphene nanocomposite as electrode materials in LIB and found that the insertion and extraction capacities of 2399 $mAhg^{-1}$ and 1176 $mAhg^{-1}$, respectively,

in the first cycle. We believe that our study sheds light on a novel synthetic approach of porous ceramic-based monoliths.

2. EXPERIMENTAL SECTION

2.1. Materials

Sulfuric acid (H_2SO_4, 98%), hydrogen peroxide (30%), graphite powder, hexadecylamine (90%), nickel acetylacetonate were purchased from Sigma Aldrich. Nickel acetylacetonate was incorporated as a crosslinking agent for the methyl polysiloxane resin. Chloroform (ASC, 99.8%), cyclohexane (ASC, 99%), dimethylsulfoxide (99%), potassium permanganate (99%), sodium nitrate (99%), chlorhydric acid (36%), were purchased from Alfar Aesar, Germany. A commercial methyl polysiloxane resin, (Silres MK) was purchased from Wacker Chemie (Munich, Germany).

2.2. Sample characterization

The infrared spectra were obtained using a Nicolet Nexus FT-IR spectrometer equipped with an ATR (Golden Gate Diamond) system in the 600 to 4000 cm^{-1} range. The morphologies of GO and nanocomposites were imaged using a Hitachi S4800 scanning electron microscope (SEM). The elemental analysis of nanocomposites was performed locally by X-ray dispersive energy (EDX) by an Oxford detector (X-Max N SDD). X-ray diffraction (Philips X'pert PRO X-ray diffraction system, with Cu-Kα radiation (λ = 0.154 nm) was used to study the crystal structure. The thermogravimetric analysis (TGA) was carried out under nitrogen on a TGA-STD Q600 thermal analysis device up to 1000 °C with a heating rate of 5 °C.min^{-1}. The size and morphology of the droplets of the emulsions were observed using an optical microscope (LEICA DM1750M). Optical microscopy measurements were performed 15 minutes after emulsification by depositing a drop

of the emulsion phase on a microscopy slide. ζ-potential was measured using Anton-Paar Litesizer 500 at 20 °C. Samples were prepared at a concentration of 3 mg/mL. The nitrogen sorption isotherms were measured with a Micromeritics ASAP 2020 analyzer at 77 K. After grinding the monoliths, the samples were degassed at 200 °C under vacuum for 12 hours before measurements were taken. The specific surface area was calculated using the Brumauer-Emmett-Teller method (BET), and the size distribution by using the Barrett-Joyner-Halenda (BJH) method.

2.3. Preparation of graphene oxide nanosheets

GO nanosheets were prepared by a modified Hummers method [32]. Briefly, the powdered natural graphite (>120 µm, 1 g) was mixed with concentrated H_2SO_4 (33.8 mL) and sodium nitrate (0.76 g). Then potassium permanganate (4.5 g) was slowly added to the mixture. A solution of sulfuric acid (100 mL) was added after 7 days. Hydrogen peroxide (3 mL) was added at the end to stop the reaction. A solution of hydrochloric acid (10%, 500 mL) was then added. The GO suspension was dialyzed in deionized water for 10 days to remove metal ions and acid. Then 50 mL of the solution was dispersed in 450 mL of water and sonicated for 30 minutes, followed by centrifugation at 3000 rpm for aggregate removal. The recovered supernatant was centrifuged at 10000 rpm to obtain a final concentration solution (7.5 mg /mL).

2.4. Modification of GO nanosheets with primary alkylamines

Graphene oxide (72.5 mg) was dispersed in 20 mL DMSO and (0.33 g) hexadecylamine dispersed in 5 mL chloroform was added dropwise with sonication. The mixture was stirred for 48 hours at room temperature and then filtered on a Polyvinylidene fluoride (PVDF) support. The final product

was washed several times with chloroform to remove non-reactive elements. The final material named GO-R16 was placed in the oven at 65°C for two hours.

2.5. Preparation of Pickering emulsions stabilized by functionalized graphene oxide

Pickering emulsions (total volume 20 mL) were prepared according to the formulation protocol described in Figure 1: (1) Functionalized graphene oxide (GO-R16) was dispersed in 10 mL cyclohexane by sonication for 10 minutes. (2) Then 10 mL DMSO was added. (3) The emulsification was carried out by a high-speed homogenizer (ultra turrax T25) for 2 minutes to form stable Pickering emulsions.

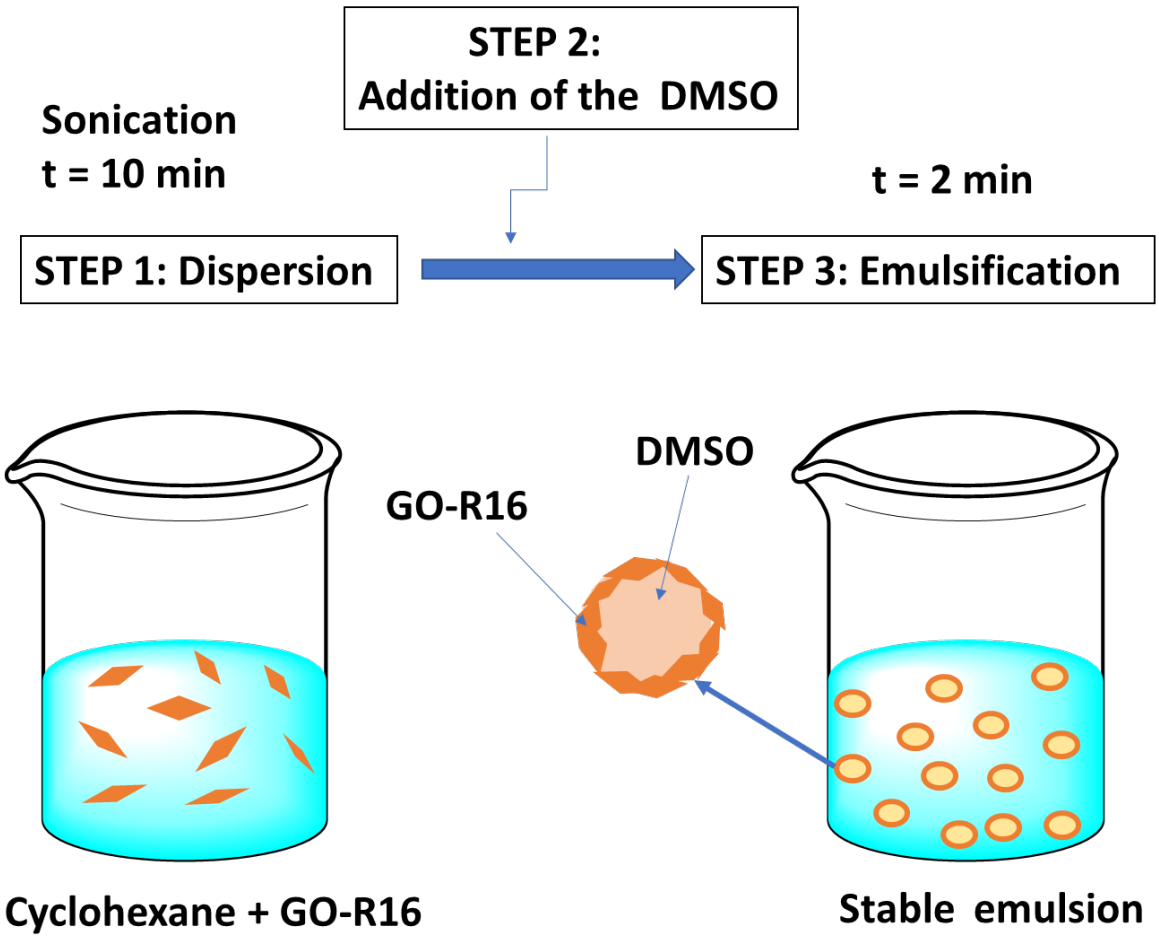

Figure 1. Schematic illustration of the preparation of the DMSO/cyclohexane Pickering emulsion stabilized with modified graphene oxide nanosheets (GO-R16)

2.6. Preparation of graphene-based polymer-derived ceramic nanocomposite

The porous monoliths were prepared via DMSO/cyclohexane Pickering emulsions combined with the polymer preceramic pathway. First, 30 mg of GO-R16 was dispersed in 3 mL cyclohexane by sonication for 10 minutes and 200, 100, 50 mg of methyl polysiloxane resin (Silres MK) received in powder form was dissolved in 2 mL cyclohexane by sonication for 2 min to produce a solution. These two solutions were then mixed, followed by sonication again for 15 minutes. Once the sonication was complete, 2 mL of a previously prepared nickel acetylacetonate containing DMSO solution of concentration 10 mg/mL was added, and the mixture was homogenized for 2 minutes at 15000 rpm. The volume fraction of DMSO and cyclohexane is 28% and 72% respectively. After a rest of 15 minutes, the emulsion was placed to freeze and then freeze-dried. This was followed by the pyrolysis of the freeze-dried material at 1°C/min up to temperatures of 600 and 900°C for 2 hours in argon atmosphere. This same procedure and condition were used to produce monoliths without nickel acetylacetonate. We have prepared nanocomposites named SiOC-GO-R16 (X, T(°C)), Ni/SiOC-GO-R16 (X, T(°C)), with X representing the mass ratio of modified GO and T(°C) referring to the pyrolysis temperature. The samples were designated as follows: SiOC-GO-R16 (38%, 900°C), SiOC-GO-R16 (23%, 900°C), and SiOC-GO-R16 (13%, 900°C) for the composites containing 50, 100, and 200 mg of methyl polysiloxane resin respectively.

2.7. Electrochemistry measurement

Electrodes were prepared by hand-mixing the active material monoliths (70 wt.%), carbon black as conducting agent (15 wt.%) (Alfa Aesar 99.9%), and polyvinylidene difluoride as binder

(15wt.%) (Alfa Aesar). Few drops of 1-Methyl-2-pyrrolidinone (Sigma Aldrich) were added until a homogeneous mixture was obtained [33]. Subsequently, a uniform thin film of approximately 125 µm was deposited on a 9 µm copper (current collector) substrate through doctor blade technique; and then dried for 18 h in oven at 80 °C for solvent removal. After drying a 7.94 mm circular punch was used to cut the composite electrodes, which were then used as a working electrode in the assembly of the CR 2023 type coin-shaped Li^+ half-cell. The cell assembly was carried out in a glove box and the counter-electrode of the assembly was pure lithium metal (diameter 14.3 mm and thickness 75 µm). The electrolyte solution used for the measurements was a mixture of 1 M lithium hexafluorophosphate ($LiPF_6$) and dimethyl carbonate (DMC) 1:1 v/v with ethylene carbonate (EC) (Sigma Aldrich). This solution had an ion conductivity of 10.7 mS cm^{-1}. A glass separator of diameter 19 mm and a thickness of 25 µm was placed between the two electrodes as they were pre-soaked with the electrolyte. The multichannel BT 2000 Arbin (College Station, TX, USA) was used for carrying out electrochemical measurements between 2.5 V and 10 mV voltage range at current densities of 50, 100, 200, 400, 600, and 800 mA g^{-1} [33].

2.8 Electrochemical Impedance Spectroscopy

Electrochemical reactions involve the transfer of electrons between two distinct chemical states. These reactions are mainly characterized by electrolyte resistance, adsorption of electroactive species, charge transfer to the electrode surface, and mass transfer of the bulk solution to the electrode surface. Electrochemical impedance spectroscopy (EIS) is a powerful tool to investigate properties of materials and Electrochemical reactions. Equivalent electrical circuit models can be envisaged to study the impedances resulting from the electrode material, the electrolyte and the current collector, generally based on physico-chemical processes [34,35]. In this study, the most essential parameters are examined in detail:

- The ohmic resistance of a cell is constituted by the ionic and electronic resistances of the electrodes, flow fields, current collectors and contact resistances. Because the impedance of a resistor only considers the real part of a complex number, the different resistances resulting from various physicochemical processes are easily identifiable from the Nyquist plot.

- The evaluation of the non-ideal surface area of the electrode is done using a constant-phase component (CPE), and the resulting impedance can be expressed as follows:

$$Z_{CPE}(\Omega) = \frac{1}{Y_0 (j\, w)^N} \quad (1)$$

$j = \sqrt{-1}$ (complex unity), w is angular frequency and N is a constant phase angle, which accounts for losses that occur in porous electrodes.

- At high frequencies, an inductive behavior caused by the movement of electrons in the potentiostat cables is observed. The resulting impedance can be calculated using the following equation:

$$Z_L(\Omega) = jwL \quad (2)$$

Where L = inductance in Ω·S

- The transport of electroactive substances by diffusion can be determined by the Warburg impedance $Z_T(\Omega)$, which is defined by the following equation:

$$Z_T(\Omega) = \frac{R\coth\,(\mathcal{J}jw)^p}{(\mathcal{J}jw)^p} \quad (3)$$

3. RESULTS AND DISCUSIONS

3.1. Characterization of functionalized graphene oxide

ATR-FTIR analysis was used as direct evidence of GO functionalization as it provides information about the functional groups present in the sample. As shown in Figure 2a, typical signatures for the GO nanosheets have been obtained with peaks at 1021 cm^{-1}, 1624 cm^{-1} and 1741 cm^{-1} corresponding to the stretching of C-O-C, C=C, C=O respectively. The peak at 3353 cm^{-1} corresponds to the vibration mode of the OH group [36] . After functionalization, we noticed the appearance of two new peaks of significant intensity at 2850 cm^{-1} and 2923 cm^{-1}, attributed to the stretching and vibration modes of the CH_2 groups, respectively, which probably arise from alkyl amine with a peak around 728 cm^{-1} [37]. An additional peak appears at 1082 cm^{-1} and is attributed to the C-N vibration mode, indicating the formation of C-ONH- bonds, corresponding to the formation of an amide bond between the alkyl amine and GO.

To further characterize the functionalization of the GO nanosheets, we performed thermogravimetric analyses (TGA). The mass loss profile of unmodified GO shows an initial loss below 100 °C when heating begins (Figure 2c). This corresponds to a loss of adsorbed water. A second mass loss is visible between 150 and 250 °C, which can be attributed to the loss of oxygenated fractions on the surface of GO [38]. The TGA curve of GO modified with hexadecylamine (GO-R16) shows a three-stage degradation profile. The main loss of around 84 %, in the temperature range 200 to 550 °C, is attributed to the decomposition of the grafted alkyl amine chain [26]. On the other hand, for R16, the decomposition takes place in the temperature range 200 – 300 °C with a residual mass of 2% at 300 °C. To confirm the presence of the functional group on the basal plan of the nanosheets, we investigated the X-ray diffraction (XRD) patterns of

thin GO films prepared by vacuum filtration [39]. Our XRD analyses show the (001) peak at 2θ = 9.7° corresponding to an interlayer distance of 0.91 nm. This finding is in agreement with the typical value cited in the literature and is attributed to the presence of water interposed between the layers of GO as well as oxygenated functional group [32]. For GO-R16, the (001) peak is displaced to a lower angle (2θ = 5.8°) which demonstrates that the interlayer distance has increased up to 1.5 nm compared to GO. This corresponds to an increased interlayer distance of ~ 0.6 nm caused by the intercalation of hexadecylamine in the graphene oxide layers (Figure 2b). This combined with the absence of diffraction signal at 0.91 points to a uniform functionalization of the basal planes of the nanosheets.

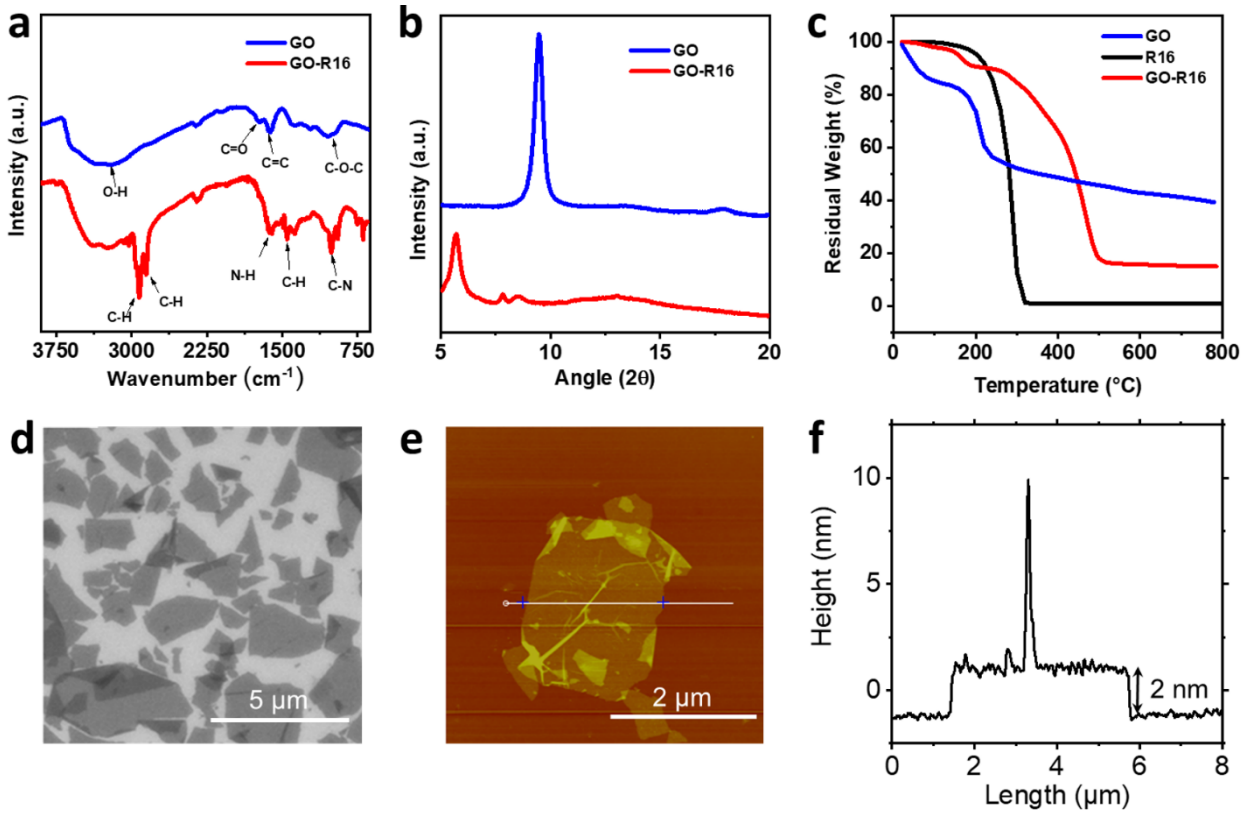

Figure 2. (a) Attenuated total reflectance Fourier transform infrared spectroscopy (ATR-FTIR) Spectra of pristine GO and modified GO nanosheets (GO-R16), (b) X-ray diffraction (XRD) patterns of GO-R16 (red), GO (blue); (c) Thermogravimetric Analysis (TGA) curves of GO-R16, GO and Hexadecylamine, (d) Scanning Electron Microscopy (SEM) image of GO-R16, (e) Atomic force microscopy (AFM) image of an individual layer of GO-R16 and (f) Corresponding height profile measurements on the AFM image of GO-R16.

To demonstrate the hydrophobic nature of GO-R16, a thin film was prepared by vacuum filtration on a PVDF porous support using a 1 mg/mL solution of the modified GO. Contact angle measurements were performed with water. Noticeably, the contact angle value increases from 47° for the unmodified graphene oxide to 97° for the graphene oxide functionalized with hexadecylamine, as shown in Figure S1b. This highlights the modification of the surface chemistry of the nanosheets thanks to the presence of the long alkyl chains of the functional groups. on confirming the successful functionalization of the GO, GO-R16 was dispersed in various polar and non-polar aprotic organic solvents. Our observations revealed that GO-R16 sheets show improved dispersion in non-polar solvents. Dispersion of nanosheets in solution reveals a charged surface with chemical composition dependent zeta potential values, as illustrated in Supplementary (Figure S2). We examined the uniformity of the dispersion by performing scanning electron microscopy (SEM) on the dispersed nanosheets drop-casted on the Si/SiO_2 wafer, and the results showed that the functionalized graphene oxide sheets are mainly present as individual single layers (Figure 2d). This observation is further supported by atomic force microscopy (AFM) images (Figure 2e). The height profile measurements from the AFM image (Figure 2f) indicate a thickness of 2 nm, which is typical for functionalized graphene oxide.

3.2. Characterization of Pickering emulsions stabilized by GO-R16

Non-aqueous emulsions were prepared by combining immiscible organic solvents. Such systems avoid the difficulties associated with the handling of water-sensitive monomers [40]. It is worth noting that among the different pre-ceramic polymer, polysiloxanes are the least water sensitive but remain poorly dispersible in water. This motivated us to identify a suitable solvent pair containing polar and non-polar aprotic solvents for the preparation of the emulsion, which are compatible with the PDC route. Obtaining non-aqueous emulsions is usually governed by the stabilizer, namely the particles at the interface, and remains a great challenge. Here, we used DMSO (dimethyl sulfoxide) and cyclohexane as organic solvents to form the non-miscible organic phases required for Pickering emulsion formation. Remarkably, DMSO and cyclohexane are also compatible with freeze-drying by adjusting temperature and pressure conditions during lyophilization [41]. Modified GO-R16 was chosen as a stabilizer in this work. To formulate the Pickering emulsions, we initially fixed the volume fraction DMSO / cyclohexane at 50%. To explore the effects of concentration, emulsification rate, emulsification time, volume ratio on Pickering emulsion stability and droplet size distribution, a series of emulsion formulations were performed under controlled experimental conditions and presented in the Table ST1.The influence of the aforementioned factors on the droplets stability and size distribution was systematically analyzed using optical microscopy.

3.2.1. Effect of emulsification speed and time on GO-R16 stabilized emulsion droplet size

To find the ideal emulsification speed, we studied the effect of the homogenization rate on the size of Pickering emulsion droplets. Several speeds were applied with the formulation conditions presented in Table ST1. The different stirring speeds chosen are 10000, 15000, 20000 and 24000

rpm. We found that it was not possible to establish a linear correlation between emulsification speed and droplet size distribution. However, in our observations, we consistently found that the average droplet size remains smaller at a speed of 15000 rpm, regardless of the concentration of GO-R16. This trend is illustrated in Figure S3. Subsequently, we explored the effect of emulsification time on the droplet size distribution for each speed used in this study. The emulsification time was tested successively for different periods (1, 2, 4 minutes). Our results demonstrate a decrease in the average droplet size over time for shearing speeds of 15000 and 10000 rpm. Particularly, at a shearing speed of 15000 rpm, the average droplet sizes as a function of time are smaller (Figure S3). However, it is important to note that the error bars in our data are relatively large, indicating the formation of emulsions with non-uniform droplet sizes. Considering the observed trends, we have decided to use a shear speed of 15000 rpm for the remainder of our studies.

3.2.2. Effect of GO-R16 concentration on the Pickering emulsion droplet size

To ascertain the presence of either cyclohexane or DMSO in the continuous phase of the emulsion, we utilized confocal fluorescence microscopy. To specifically identify the presence of DMSO, we employed Nile red (NR), a fluorescent dye that is solely soluble in DMSO (Inset Figure 3a). on examination, Nile red dissolved in DMSO was indeed found in the droplets, confirming the presence of DMSO as the dispersed phase. In contrast, cyclohexane was observed to constitute the continuous phase of the emulsion (Figure 3a). This suggests that GO-R16 nanosheets wrap well the DMSO droplets and thus stabilize the emulsion. As shown in Table S1, we investigated different concentrations of functionalized graphene oxide (GO-R16) ranging between 0.5 and 6 mg/mL (Figure 3b-e). The diameter of the emulsion droplets was systematically measured for the different DMSO/cyclohexane emulsions and the droplet size distribution of the emulsions for the

different concentrations of GO-R16 was determined (Figure S4). Our results indicate that as the amount of functionalized graphene oxide (GO-R16) increases, the droplet size decreases with a narrower size distribution. Specifically, we observed that when the concentrations of functionalized graphene oxide (GO-R16) varied from 0.5 to 6 mg/mL, the average droplet size decreases from approximately 155 μm to 35 μm. This finding suggests that higher concentrations of GO-R16 lead to the formation of smaller emulsion droplets in agreement with the literature [42,43]. The stability of an emulsion is typically influenced by four main mechanisms: sedimentation, creaming, flocculation, and coalescence. In our emulsion stability tests using GO-R16 as the stabilizer, we observed that the emulsions showed minimal changes over 24 hours, indicating high stability against droplet coalescence and creaming [43]. The creaming index is based on the total volume and is a visual test that allows one to see the presence or not of a phenomenon of destabilization of the emulsion. The creaming index was calculated by measuring the height of the clarified layer and dividing it by the total height of the emulsion. Figures 3b-e display the evolution of the droplet size when increasing the concentration of functionalized graphene oxide (GO-R16). We systematically analyzed the optical microscope observations of the Pickering emulsion. Our findings reveal that the creaming index increases with the concentration of functionalized graphene oxide (GO-R16), likely due to the related increase in viscosity (Figure 3f) [42].

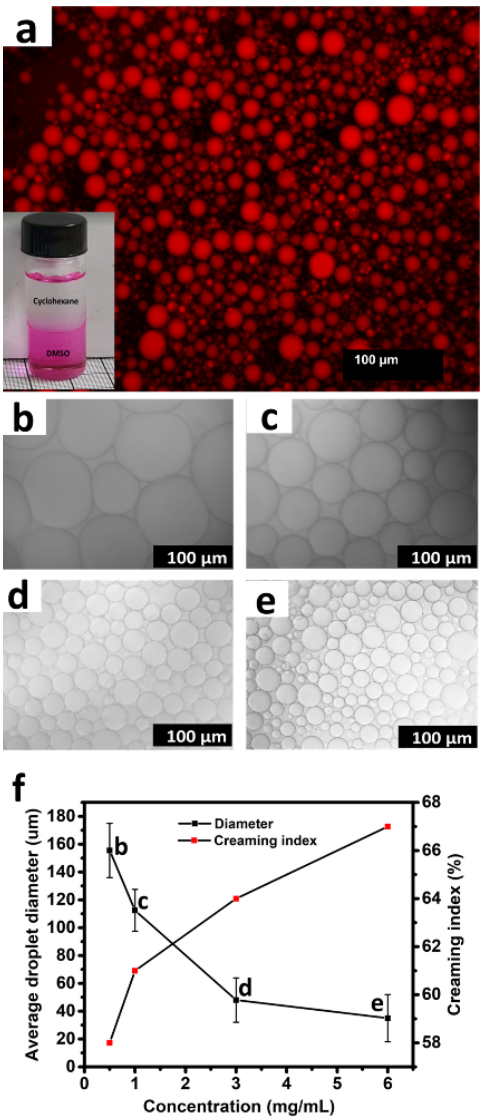

Figure 3. (a) Confocal optical microscope image in fluorescence mode of the DMSO/cyclohexane emulsion in presence of Nile Red (NR), the inset shows the solubility of NR in DMSO. (b-e) Optical microscope images of the droplet size distribution of Pickering emulsions with different concentrations of GO-R16: (b= 0.5 mg/mL, c = 1 mg/mL, d = 3 mg/mL, e = 6 mg/mL). (f) Relationship between the average droplet size and the creaming index and concentration in GO-R16

3.3. Characterization of porous graphene-based polymer-derived ceramics monoliths

The preparation of porous monoliths was carried out using Pickering emulsions based on DMSO (dimethyl sulfoxide) and cyclohexane, combined with the polysiloxane preceramic polymer. The polysiloxane was used as precursor of SiOC ceramics and is soluble in cyclohexane, *i.e.* the continuous phase of the emulsion. The formulated Pickering emulsions were observed under an optical microscope and are shown in Figures 4a-b. A diminution in droplet size is detected at higher concentration of the polysiloxane preceramic polymer, due to the larger viscosity of the continuous phase.

The pyrolysis was performed by heating the samples at a rate of 1°C/min until reaching specific temperatures, either 600° or 900°C under argon to form ceramer and ceramic monoliths respectively. The samples were held at these temperatures for 2 hours under argon. After pyrolysis the morphology of the monoliths was characterized by SEM as displayed in Figures 4c-d. Figures 4e-f shows SEM images of the same samples prepared in presence of nickel acetylacetonate used as crosslinker of the pre-ceramic polymer. We found that the monoliths consist of interconnected pores with almost spherical and non-homogeneous open cavities. These open channels reflect the shape of the DMSO droplets in the continuous phase and confirm that the droplets can be preserved after sublimation and ceramization. The non-homogeneous morphology of the cavities is attributed to the coalescence [43] of the droplets before and during the freeze-drying step. Similarly, the SEM images in Figure 4e-f of the monoliths with nickel acetylacetonate show an open-cell macroporous structure resulting from the initial drops, which proves that the Pickering emulsion acts as a soft template. The ATR-FTIR analysis in Figure S7a shows the presence of peaks corresponding to the presence of the different chemical bonds of the methyl polysiloxane resin and the resulting SiOC ceramics. The peaks at 2917 and 2850 cm^{-1} correspond to the C-H stretching vibration. The strong

peaks in the range 1038 -1089 cm^{-1} are attributed to the Si-O-Si bridge vibration. The bands at 1272, 860 and 760 cm^{-1} correspond to the stretching of Si-CH_3, Si-OH, Si-C respectively. After the pyrolysis, we notice the presence of a peak at 1507 cm^{-1} reflecting the presence of the C = C bond. In contrast, only Si-O-Si and Si-C stretching vibrations at 1010 and 795 cm^{-1} remain visible in the samples ceramized at 900 °C, indicating that the process was complete [44]. Figure S6b-c shows the TGA of various polysiloxane resin compositions used in the formulation of Pickering emulsions, highlighting the transformation of the polymer into ceramics. We estimated the ceramic yield at 1000°C for the pure polysiloxane precursor to be approximately 82%. SiOC-GO-R16 composites showed overall mass losses of the order of 35, 30, 44% at 1000 °C for samples containing 23, 13, 38 % of the functionalized graphene oxide (GO-R16). The lower mass losses of composites of the emulsions compared to pristine polysiloxane is attributed to the reduction of graphene oxide and the loss of the functional groups. We also examined the mass loss for the composites with the incorporation of nickel acetylacetonate and did not observe a significant difference. But the samples containing 23% of functionalized graphene oxide (GO-R16) showed a residual mass of 72% at 1000°C, corresponding to a mass loss of 28%, which is attributed to the decomposition of the crosslinking agent and the reduction of graphene oxide.

To provide information on the crystalline state of ceramics, we performed XRD analyses on the composites with and without the addition of nickel acetylacetonate pyrolyzed at 900 °C (Figure S7d-i). The diagram shows a wide diffraction signal in the 2θ interval between 8 - 30° corresponding to the formation of an amorphous structure associated with the SiOC matrix [45]. After pyrolysis, the diffractograms of samples containing nickel acetylacetonate in the dispersed phase showed peaks (2θ = 39°; 44°; 48°) indicating the formation of crystalline metallic nickel particles [44]. This suggests that Ni^{+}(II) was reduced to form Ni (0) nanoparticles. The presence of

nickel in the SiOC matrix was further confirmed by the EDX analyses (Figure S8). To better characterize the nickel particles, transmission electron microscopy (TEM) investigations were carried out. The TEM images show nanoclusters of nickel nanoparticles embedded in the amorphous matrix of Ni/SiOC-GO-R16 (23%, 900 °C) with an average diameter of 67 nm (Figure S8g) [46]. In addition, a sub-multilayer and sandwich structure consisting of carbon planes probably present in the amorphous SiOC-GO-R16 matrices is noticed (Figure S8h). This indicates the presence of graphene layers [47]. The XPS analyses provided information on the samples, enabling us to identify the functionalized groups present in the material, the chemical species, the bonds and the chemical states, as described in Supplementary Information (Figure S11).

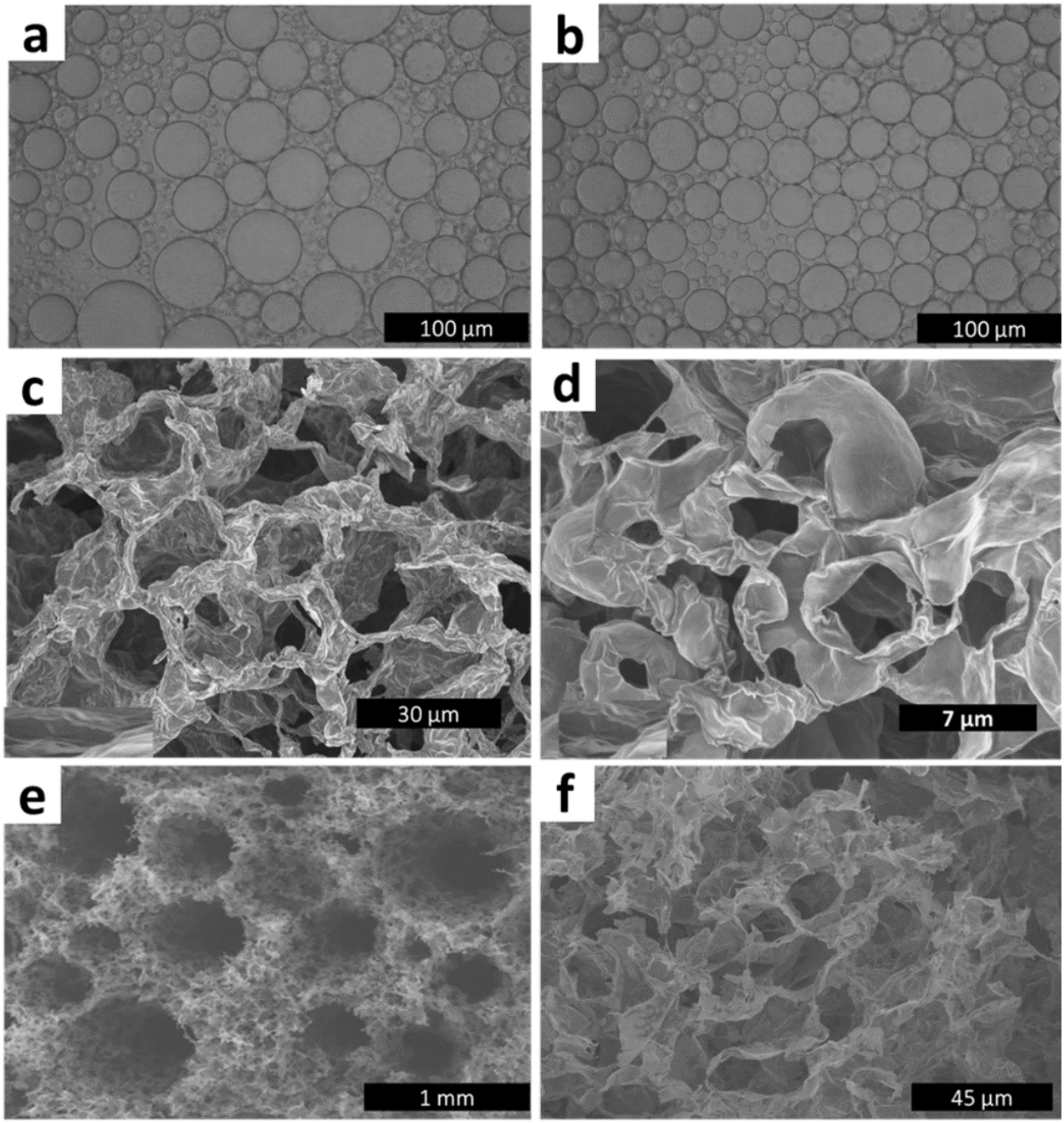

Figure 4. (a-b) Optical microscope images of Pickering emulsions after addition of methyl polysiloxane resin (a = 38%, b = 23% of functionalized graphene oxide (GO-R16)) and (c-d) Scanning electron microscopy (SEM) images of the porous structure of composites for different formulations (c = 38%, d = 23% of functionalized graphene oxide (GO-R16)) after ceramization, (e-f): Scanning Electron Microscopy (SEM) images of the porous structure of composites for

different formulations (e = 38%, f = 23% functionalized graphene oxide (GO-R16)) in the presence of nickel acetylacetonate after ceramization

To better characterize the monoliths, we then investigated the microporosity of the composite ceramics. The adsorption and desorption behavior determined by BET is illustrated in Figures 5a-b and (Figure S12). All composite samples exhibit a hysteresis loop in the N_2 adsorption isotherms, revealing the mesoporous nature of the pores. On the contrary, pure SiOC (900°C) sample does not possess any porous structure. The hysteresis indicates a network of pores consisting of macropores that are not completely filled with pore condensate [48]. According to the IUPAC classification, the isotherms are of type IV with distinct H4 type hysteresis loops at the relative pressure p/p_0 of 0.42. According to the analysis of the pore size distribution by the BJH method for the ceramic monoliths pyrolyzed at 900°C, we detected macro-size pores (> 50 nm) and meso-size pores (2-50 nm) (Figure 5c-d). We observed that the largest number of pores is distributed at about 4 nm for most other samples suggesting a dominating mesoporosity. Our BET study also indicates a clear overall increase in specific surface area (SSA) of 10 % on average after introduction of nickel acetylacetonate (Figure S13) in agreement with previous results from the literature [14]. This result confirms the beneficial effect of nickel acetylacetonate in preventing the collapse of the porosity [45]. The effect of temperature on the specific surface of the monoliths was then investigated. Our results show that the samples pyrolysed at 600°C showed higher specific surfaces than those pyrolysed at 900°C. The apparent low specific surface values (SSA) could be related to the pyrolysis conditions as previously reported by Colombo and al. [16]. The increase in surface area after pyrolysis at 600°C is attributed to transient porosity during the polymer-ceramic conversion, which typically disappears at temperatures above 900°C. Taken together, our results demonstrated the successful preparation of porous silicon oxycarbide/Graphene Oxide (SiOC-GO-

R16) porous monoliths using the Pickering emulsion route. The presence of mesopores and macropores in the SiOC-GO-R16 (900°C) and Ni/SiOC-GO-R16 (900°C) samples, along with the incorporation of conducting reduced graphene oxide (rGO) nanosheets, suggests potential benefits for utilizations as battery anode by providing active lithium-ion storage sites and facilitating the diffusion of the electrolyte [49].

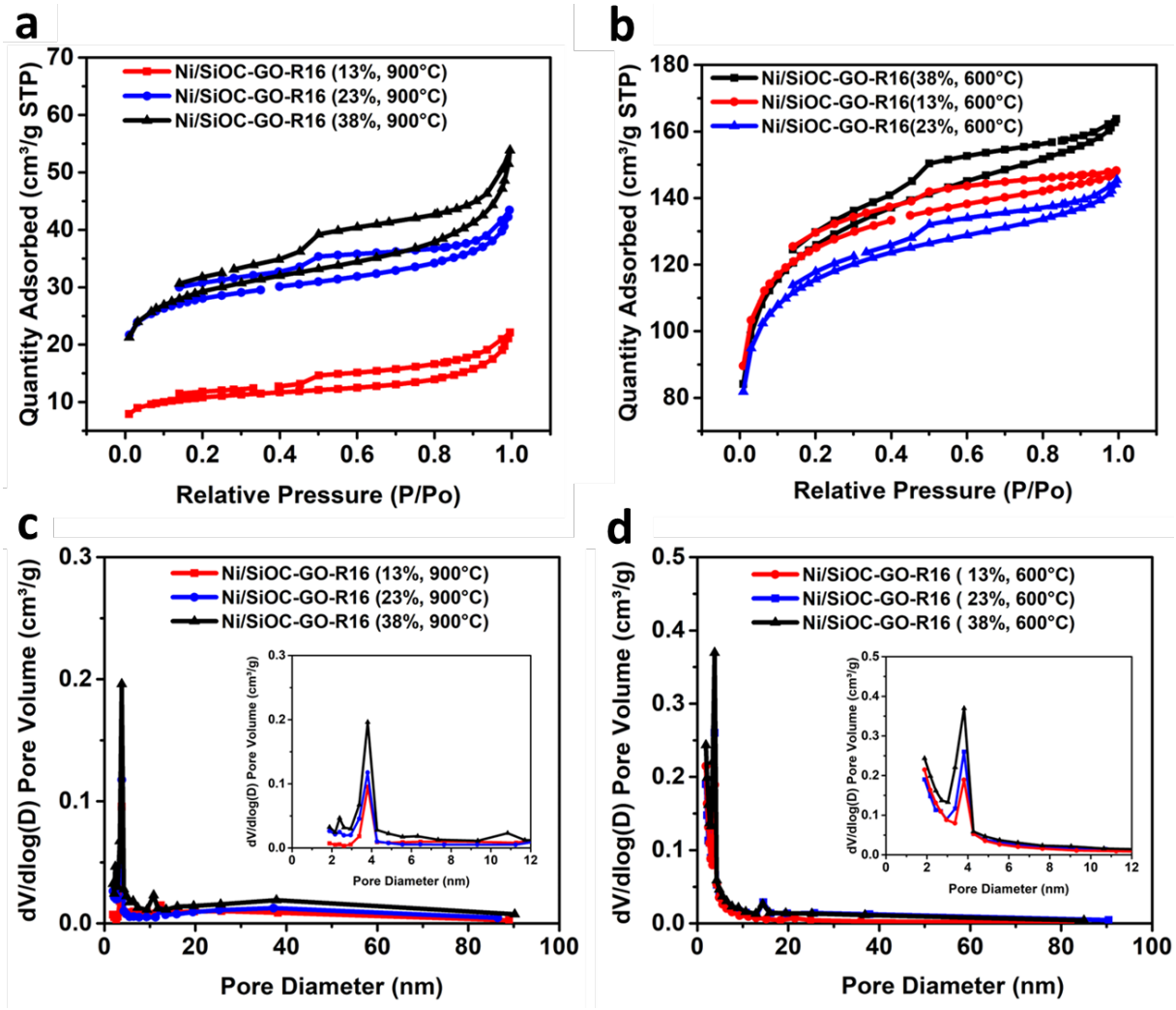

Figure 5. (a-b) N_2 adsorption/desorption isotherms for Ni/SiOC-GO-R16 (X, T(°C)) composites pyrolyzed at 900°C and 600°C and (c-d) Pore size distribution of Ni/SiOC-GO-R16 (X, T(°C)) composites pyrolysed at 900°C and 600°C

3.4. Electrochemical properties

We investigated the electrochemical properties of porous composite ceramics used as Li^+-ion battery anode, focusing on the Li^+ insertion/extraction behavior.

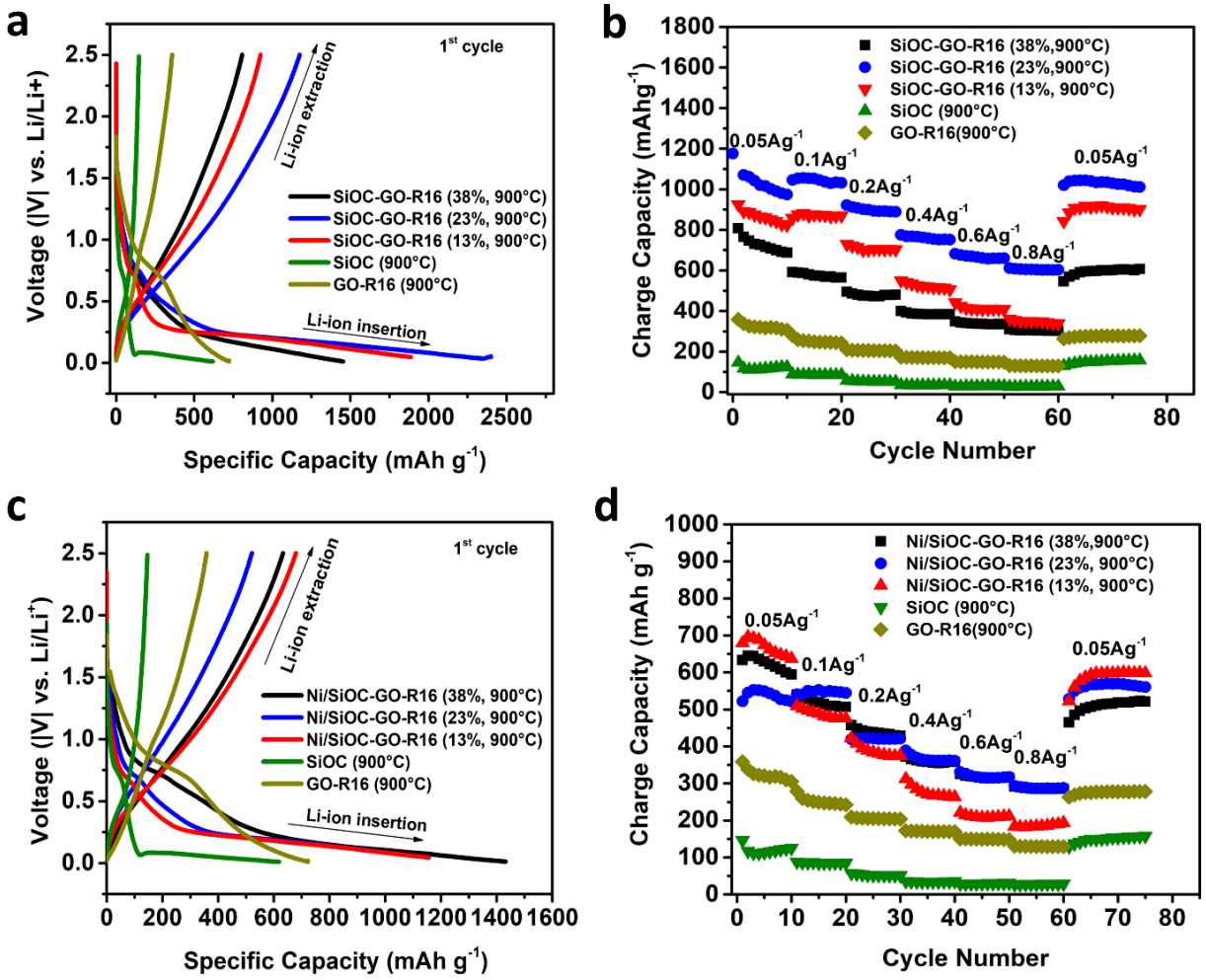

Figure 6. (a) charge/discharge profile for 1st cycle at 50 mA g^{-1} of composite samples SiOC-GO-R16 (X, T(°C)), GO-R16 (900 °C) and SiOC (900 °C) pure, (b) cycling performance of composite samples SiOC-GO-R16 (X, T(°C)), GO-R16 (900 °C) and SiOC (900 °C) pure with increasing current rates, (c) charge/discharge profile for 1st cycle at 50 mA g^{-1} of composite samples Ni/SiOC-GO-R16 (X, T(°C)), GO-R16 (900 °C) and SiOC pure and (d) cycling performance of composite samples Ni/SiOC-GO-R16 (X, T(°C)), GO-R16 (900 °C) and SiOC (900 °C) pure

Figure 6a represents the first cycle Li^+-ion insertion/extraction curves of the SiOC-GO-R16 (900 °C) porous, SiOC (900 °C) nonporous and GO-R16(900 °C) anodes, respectively at a current density of 50 mA g^{-1}. To observe small transitions in the voltage profiles by transforming plateaus into peaks, we performed differential capacity analyses (dQ/dV vs. voltage) (Figure S14). The differential capacity curves of the SiOC-GO-R16 (900 °C) and non-porous SiOC (900 °C) composite electrodes showed distinct peaks during the first cycle of lithium insertion [33]. These peaks can be attributed to the decomposition of the electrolyte and the formation of the solid electrolyte interface (SEI) during the initial Li^+-ion insertion process [50]. Remarkably, in the second cycle, the shape of the differential capacity curves remained consistent for all samples, with no peaks observed, indicating that the SEI had already been formed in agreement with previous observations.

The SiOC-GO-R16 (23%, 900 °C) electrode shows an initial Li^+-ion insertion/extraction capacity of approximately 2400 mAh g^{-1} and 1176 mAh g^{-1} respectively during the first cycle. These values represent some of the highest performances reported for silicon oxycarbide (SiOC)/rGO composite electrodes in the literature (Table S3), highlighting the excellent electrochemical properties of our synthesized material. The SiOC-GO-R16 (23%, 900 °C) electrode had a coulombic efficiency of 49%. In addition, the SiOC-GO-R16 (23%, 900 °C), SiOC-GO-R16 (13%, 900 °C), SiOC-GO-R16 (38%, 900 °C) electrodes all showed a large irreversible loss of capacity (Table S3), which corresponds to the difference between the first Li^+-ion insertion and first Li^+-ion extraction. The irreversible loss of capacity in the first cycle is typically observed for silicon oxycarbide anodes and is attributed to several major phenomena: (1) electrolyte decomposition; (2) the formation of a solid electrolyte interface (SEI) during the Li^+-ion insertion process [51]; (3) specific surface areas.

For comparison, we also tested non-porous SiOC (900 °C) and GO-R16 (900 °C) electrodes and observed an initial insertion capacity of only 619, 723 mAh g^{-1} and an initial extraction capacity of 146, 359 mAh g^{-1} with a coulombic efficiency of about only 23% and 50% respectively in the first cycle. The results of Table S3 suggest that the best coulombic efficiency and the lowest irreversible capacity are obtained for the SiOC-GO-R16 (38%, 900 °C) sample with a coulombic efficiency of about 55%. After the first cycle the coulombic efficiency of all the samples gradually increased to 99% (Figure S15). We then examined the cycling performance of the SiOC-GO-R16 (900 °C), SiOC (900 °C) and GO-R16 (900 °C) electrodes at different insertion/extraction current densities, illustrating the cycling behavior of composites for different preceramic polymer contents (Figure 6b). For the initial cycle a slow charge/discharge current rate of 50 mA g^{-1} was used, after each 10 cycles the current density was increased up to 100, 200, 400, 600, 800 mA g^{-1} and then decreased to 50 mA g^{-1} after 60 cycles. When the electrodes have been further cycled with increasing current densities, a decrease in charge capacity is observed. For example, at 800 mA g^{-1} in the 60th cycle, the charging capacity of SiOC-GO-R16 (23%, 900 °C) dropped to 603 mAh g^{-1} corresponding to 51% of its initial capacity at 50 mA g^{-1}. Regarding the SiOC-GO-R16 (38%, 900 °C), SiOC-GO-R16 (13%, 900 °C) electrodes the average charge capacity is about 304, 338 mAh g^{-1} (37 and 36%) of the initial charge capacity respectively. For the pure SiOC (900 °C) anode, the charging capacity fades up to 28 mAh g^{-1}. After 60 cycles the GO-R16 (900 °C) electrode shows a charging capacity of more than 120 mAh g^{-1}. When the density is reduced to 50 mAh g^{-1}, the SiOC-GO-R16 (23%, 900 °C) electrode fully recovers, displaying a reversible capacity of approximately 1119 mAh g^{-1}. Among the other tested electrodes, the SiOC-GO-R16 (38%, 900 °C), SiOC-GO-R16 (13%, 900 °C), SiOC (900 °C) pure, and GO-R16 (900 °C) electrodes retain 68, 91, 88, and 73% of their initial capacity, respectively. The SiOC-GO-R16

(23%, 900 °C) electrode exhibits an exceptional restoration of the insertion performance, with a good 95% retention. This result indicates excellent stability against multiple electrochemical cycles, with no significant damage to the electrode structure even under high-rate cycling conditions. Additionally, it is worth noting that there is no linear dependence between the electrochemical performance and the amount of preceramic polymer added, highlighting the complex interplay of factors influencing the material's behavior.

We then scrutinized the influence of nickel acetylacetonate on the electrochemical performance of SiOC-GO-R16 electrodes by comparing the Li^+ insertion/extraction behavior of Ni/SiOC-GO-R16 (900 °C) and SiOC-GO-R16 (900 °C) samples. Although the introduction of nickel acetylacetonate improves the specific surface area, it should be noted that the incorporation of nickel acetylacetonate in the SiOC-GO-R16 matrix does not significantly improve the lithium insertion capacity in the first cycle of SiOC-GO-R16 (900 °C) composite anodes. We finally examined the role of the porosity on the electrode storage capacity. It can be observed that the introduction of the porosity improves the insertion capacity during the first cycle for the porous SiOC-GO-R16 (900 °C) electrode compared to the non-porous SiOC (900 °C). The improved performance of the porous electrodes can be attributed to the interconnected networks of macro and mesopores. Additionally, the porous structure facilitates shorter diffusion pathways, allowing for faster ion movement and enhancing ion transport [52]. Our results also reveal that further increasing the surface area does not result in improved capacitance beyond a value of the specific surface area of 11 $m^2 g^{-1}$ (Figure S16). Overall, our study underscores the importance of optimizing the porosity and surface area to achieve the best possible electrochemical performance for porous ceramic electrodes [52].

3.5. Electrochemical impedance spectroscopy

The Li^+-ion storage behavior within neat and composite ceramic electrodes was further highlighted utilizing EIS analysis. In this study, EIS spectra of all the cells were obtained after 76th cycle discharge (presented as Nyquist plots in Figure 7), after ensuring complete relaxation when the open-circuit voltage of the cells reached 0.1 V. Obtaining data in such a manner ensures the clarity of the EIS spectra, without any anomalies and noise generation. All the acquired spectra were additionally fitted using Zview software (v3.2b, Copyright Scribner Associates, Inc., Southern Pines, NC, USA) for quantitative analysis and displayed in Table S4.

An inductive behavior is observed in the high-frequency range for all the spectra due to the measurement system (connection of wires from the half-cell and potentiostat) and is fitted using an inductive element L in the equivalent circuit model shown in Figure S18. The inductive loop next intersects the real impedance axis, which is denoted as electrolyte resistance (R_{ohm}). A general trend of increase in electrolyte resistance was observed as a function of precursor amount. For example, the highest resistance from the electrolyte was realized for the SiOC-GO-R16 (38%, 900°C) sample, while the SiOC-GO-R16 (13%, 900°C) electrode showed the least electrolyte resistance in the same group. A small flat depressed semicircle is present next in the spectra, denoting the impedance of SEI formation, and is fitted utilizing an R|Q element (parallel CPE and R_{SEI} element). Notably, R_{SEI} values for the SiOC-GO-R16 (23%, 900°C) (22.02 ohm) and Ni/ SiOC-GO-R16 (13%, 900°C) (14.94 ohm) electrodes were the lowest among the two sets of composite electrodes, which also reflected better capacity in the cycling test shown in Figure 6 (b, and d). Mid-frequency second depressed semi-circle in Figure 7 was ascribed to the charge-transfer phenomena and fitted with another resistor (R_{CT}) and constant phase element (CPE_{dl}) in parallel shown in Figure S18. The CPE_{dl}-N values for all the electrodes were around 0.9, indicating a porous electrode's surface capacitive-type charge storage behavior for all the electrodes [53]. The charge transfers resistance (R_{CT}) values for all the electrodes were considerably high. This high value can be correlated to the aging mechanism of the cells contributing to morphological changes, particle cracking, and particle disconnection with the current collector due to the repeated cycling process [54,55]. The tail of the Nyquist plots for all the electrodes indicates finite space type Warburg impedance reflecting solid-state diffusion. For all the electrodes in this study, the W-P values were around 0.4, which is a slight deviation from the ideal value of 0.5 or 45° inclination of the tail.

This deviation might result from the ion diffusion in the electrolyte phase. Therefore, diffusion coefficient determination from the W-ζ value is also avoided, as the diffusion would be a result of mixture from both solid and electrolyte phase diffusion [56]. Furthermore, the W-R values indicating the diffusion resistances were highest for the SiOC-GO-R16 (13%, 900°C) and Ni/SiOC-GO-R16 (38%, 900°C) electrodes, which can be well corroborated with the low capacity retention observed in Figure 6.

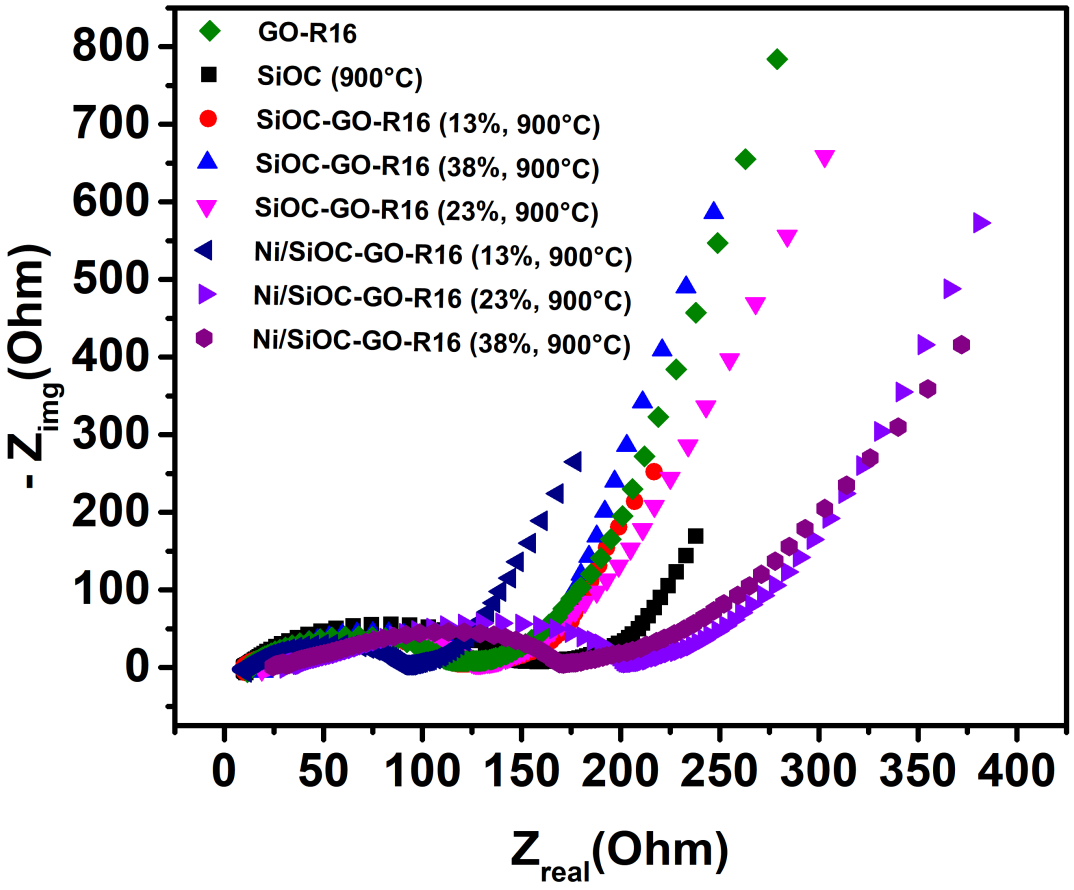

Figure 7: Real vs. imaginary impedance (Nyquist) plots of electrodes after 76th cycle discharge.

4. CONCLUSION

We demonstrated the preparation of graphene-based silicon oxycarbide composites with hierarchical porosity, interconnected pores and an open cavity. This was achieved by combining the PDCs route and the non-aqueous Pickering emulsion method in DMSO/cyclohexane stabilized by functionalized graphene oxide nanosheets (GO-R16). This synthetic route enables the preparation of porous conducting ceramic-based nanocomposites with tunable specific surface area, which have been utilized as working electrodes for Li^+-ion half-cells. Regarding the electrochemical properties, the SiOC-GO-R16 (23%, 900 °C) electrode with a surface area of 11 $m^2\ g^{-1}$ demonstrated a charge capacity of 1176 mAh g^{-1} in first cycle at 50 mA g^{-1} and 350 mAh g^{-1} at current densities of 800 mA g^{-1} after 245 cycles. The porous structure and the incorporation of graphene oxide in the SiOC matrix contributed to the improvement in charge/discharge capacity. Our study highlights the advantages of Pickering emulsions in preparing porous electrodes, although further optimization is required to fully harness their potential and address challenges associated with irreversible capacitance loss of the first cycle. Our findings pave the way for the development of high-performance porous ceramic electrodes with potential applications in energy storage devices.

AUTHOR INFORMATION

Corresponding Author

Philippe Miele - Institut -Européen des Membranes (IEM), UMR 5635, Université de Montpellier, ENSCM, CNRS, Montpellier, France

Email : philippe.miele@umontpellier.fr

Chrystelle Salameh -Institut Européen des Membranes (IEM), UMR 5635, Université de Montpellier, ENSCM, CNRS, Montpellier, France

Email : Chrystelle.Salameh@enscm.fr

Authors

Damien Voiry - Institut Européen des Membranes (IEM), UMR 5635, Université de Montpellier, ENSCM, CNRS, Montpellier, France

Bonito A. Karamoko - Institut Européen des Membranes (IEM), UMR 5635, Université de Montpellier, ENSCM, CNRS, Montpellier, France

Wensen Wang - Institut Européen des Membranes (IEM), UMR 5635, Université de Montpellier, ENSCM, CNRS, Montpellier, France

Jiefeng Liu - Institut Européen des Membranes (IEM), UMR 5635, Université de Montpellier, ENSCM, CNRS, Montpellier, France

Sonjoy Dey - Department of Mechanical and Nuclear Engineering, Kansas State University, Manhattan, KS 66506, USA

Shakir Bin Mujib - Department of Mechanical and Nuclear Engineering, Kansas State University, Manhattan, KS 66506, USA

Gurpreet Singh - Department of Mechanical and Nuclear Engineering, Kansas State University, Manhattan, KS 66506, USA

Ji Li - College of Bioresources and Materials Engineering, Shaanxi University of Science and Technology, Xi'an, People's Republic of China

Benjamin K. Yao -Laboratory of Synthesis, Industrial Processes, Environment, and Renewable Energies, Félix Houphouët-Boigny National Polytechnic Institute of Yamoussoukro, P.O. Box 1093, Yamoussoukro, Ivory

Author Contributions

BAK conducted the experiments, analyzed the data and prepared the manuscript. WW, JF, and JL contributed to the characterization of the materials properties. SD, GS, SBM contributed to the electrochemical measurements. BKY, CS, DV and PM designed and supervised the study, analyzed the data and prepared the manuscript. All authors discussed the results and commented on the manuscript.

Notes

The authors declare no competing financial interests.

ACKNOWLEDGMENT

This work was supported by the Ministry of Higher Education and Scientific Research (MESRS) of the Republic of Côte d'Ivoire. Financial support from US National Science Foundation (NSF) Partnerships for International Research and Education (PIRE) grant number 1743701 is gratefully acknowledged. French National Agency (ANR), Grant Number: ANR-20-CE08-0009 (MONOME project) and Axe Energie, IEM (Solid-CeraLique project, axe transverse PAT) and IUF are acknowledged for funding.

REFERENCES

(1) Vakifahmetoglu, C.; Zeydanli, D.; Colombo, P. Porous Polymer Derived Ceramics. *Materials Science and Engineering R: Reports* **2016**, *106*, 1–30. https://doi.org/10.1016/j.mser.2016.05.001.

(2) Kumar, B. V. M.; Kim, Y. W. Processing of Polysiloxane-Derived Porous Ceramics: A Review. *Sci Technol Adv Mater* **2010**, *11* (4). https://doi.org/10.1088/1468-6996/11/4/044303.

(3) Pickering SU. CXCVI. –Emulsions. . *Chem. Soc., Trans.,* **1907**, *91*, 2001–2021. https://doi.org/10.1039/CT9079102001.

(4) Schmitt, V.; Destribats, M.; Backov, R. Colloidal Particles as Liquid Dispersion Stabilizer: Pickering Emulsions and Materials Thereof. *C R Phys* **2014**, *15* (8–9), 761–774. https://doi.org/10.1016/j.crhy.2014.09.010.

(5) Zheng, Z.; Zheng, X.; Wang, H.; Du, Q. Macroporous Graphene Oxide-Polymer Composite Prepared through Pickering High Internal Phase Emulsions. *ACS Appl Mater Interfaces* **2013**, *5* (16), 7974–7982. https://doi.org/10.1021/am4020549.

(6) Ji, X.; Wang, S.; Shao, C.; Wang, H. High-Temperature Corrosion Behavior of SiBCN Fibers for Aerospace Applications. *ACS Appl Mater Interfaces* **2018**, *10* (23), 19712–19720. https://doi.org/10.1021/acsami.8b04497.

(7) Salameh, C.; Bruma, A.; Malo, S.; Demirci, U. B.; Miele, P.; Bernard, S. Monodisperse Platinum Nanoparticles Supported on Highly Ordered Mesoporous Silicon Nitride Nanoblocks: Superior Catalytic Activity for Hydrogen Generation from Sodium Borohydride. *RSC Adv* **2015**, *5* (72), 58943–58951. https://doi.org/10.1039/c5ra05901a.

(8) Lale, A.; Wasan, A.; Kumar, R.; Miele, P.; Demirci, U. B.; Bernard, S. Organosilicon Polymer-Derived Mesoporous 3D Silicon Carbide, Carbonitride and Nitride Structures as Platinum Supports for Hydrogen Generation by Hydrolysis of Sodium Borohydride. *Int J Hydrogen Energy* **2016**, *41* (34), 15477–15488. https://doi.org/10.1016/j.ijhydene.2016.06.186.

(9) Majoulet, O.; Salameh, C.; Schuster, M. E.; Demirci, U. B.; Sugahara, Y.; Bernard, S.; Miele, P. Preparation, Characterization, and Surface Modification of Periodic Mesoporous

Silicon-Aluminum-Carbon-Nitrogen Frameworks. *Chemistry of Materials* **2013**, *25* (20), 3957–3970. https://doi.org/10.1021/cm401605a.

(10) Bernard, S.; Miele, P. Ordered Mesoporous Polymer-Derived Ceramics and Their Processing into Hierarchically Porous Boron Nitride and Silicoboron Carbonitride Monoliths. *New Journal of Chemistry* **2014**, *38* (5), 1923–1931. https://doi.org/10.1039/c3nj01612a.

(11) Arango-Ospina, M.; Xie, F.; Gonzalo-Juan, I.; Riedel, R.; Ionescu, E.; Boccaccini, A. R. Review: Silicon Oxycarbide Based Materials for Biomedical Applications. *Applied Materials Today*. 2020. https://doi.org/10.1016/j.apmt.2019.100482.

(12) Hwang, Y.; Riu, D. H.; Kim, K. J.; Chang, C. H. Porous SiOC Beads by Freeze-Drying Polycarbosilane Emulsions. *Mater Lett* **2014**, *131*, 174–177. https://doi.org/10.1016/j.matlet.2014.05.194.

(13) Bakumov, V.; Schwarz, M.; Kroke, E. Emulsion Processing of Polymer-Derived Porous Si/C/(O) Ceramic Bodies. *J Eur Ceram Soc* **2009**, *29* (13), 2857–2865. https://doi.org/10.1016/j.jeurceramsoc.2009.04.004.

(14) Schlüter, F.; Meyer, J.; Wilhelm, M.; Rezwan, K. Hierarchical Emulsion Based Hybrid Ceramics Synthesized with Different Siloxane Precursor and with Embedded Nickel Nanoparticles. *Colloids Surf A Physicochem Eng Asp* **2016**, *492*, 160–169. https://doi.org/10.1016/j.colsurfa.2015.12.020.

(15) Moni, P.; Chaves, W. F.; Wilhelm, M.; Rezwan, K. Polysiloxane Microspheres Encapsulated in Carbon Allotropes: A Promising Material for Supercapacitor and Carbon Dioxide Capture. *J Colloid Interface Sci* **2019**, *542*, 91–101. https://doi.org/10.1016/j.jcis.2019.01.087.

(16) Naglieri, V.; Colombo, P. Ceramic Microspheres with Controlled Porosity by Emulsion-Ice Templating. *J Eur Ceram Soc* **2017**, *37* (7), 2559–2568. https://doi.org/10.1016/j.jeurceramsoc.2017.02.033.

(17) Vakifahmetoglu, C.; Balliana, M.; Colombo, P. Ceramic Foams and Micro-Beads from Emulsions of a Preceramic Polymer. *J Eur Ceram Soc* **2011**, *31* (8), 1481–1490. https://doi.org/10.1016/j.jeurceramsoc.2011.02.012.

(18) Huang, X.; Yang, J.; Mao, S.; Chang, J.; Hallac, P. B.; Fell, C. R.; Metz, B.; Jiang, J.; Hurley, P. T.; Chen, J. Controllable Synthesis of Hollow Si Anode for Long-Cycle-Life Lithium-Ion Batteries. *Advanced Materials* **2014**, *26* (25), 4326–4332. https://doi.org/10.1002/adma.201400578.

(19) Pradeep, V. S.; Ayana, D. G.; Graczyk-Zajac, M.; Soraru, G. D.; Riedel, R. High Rate Capability of SiOC Ceramic Aerogels with Tailored Porosity as Anode Materials for Li-Ion Batteries. *Electrochim Acta* **2015**, *157*, 41–45. https://doi.org/10.1016/j.electacta.2015.01.088.

(20) Dibandjo, P.; Graczyk-Zajac, M.; Riedel, R.; Pradeep, V. S.; Soraru, G. D. Lithium Insertion into Dense and Porous Carbon-Rich Polymer-Derived SiOC Ceramics. *J Eur Ceram Soc* **2012**, *32* (10), 2495–2503. https://doi.org/10.1016/j.jeurceramsoc.2012.03.010.

(21) Xia, K.; Liu, X.; Liu, H.; Lu, Y.; Liu, Z.; Li, Y.; Duan, L.; Hou, Z.; Li, R.; Wang, D. Carbon-Enriched SiOC Ceramics with Hierarchical Porous Structure as Anodes for Lithium Storage. *Electrochim Acta* **2021**, *372*, 137899. https://doi.org/10.1016/j.electacta.2021.137899.

(22) David, L.; Bhandavat, R.; Barrera, U.; Singh, G. Silicon Oxycarbide Glass-Graphene Composite Paper Electrode for Long-Cycle Lithium-Ion Batteries. *Nat Commun* **2016**, *7*, 10998. https://doi.org/10.1038/ncomms10998.

(23) Sang, Z.; Zhao, Z.; Su, D.; Miao, P.; Zhang, F.; Ji, H.; Yan, X. SiOC Nanolayer Wrapped 3D Interconnected Graphene Sponge as a High-Performance Anode for Lithium Ion Batteries. *J Mater Chem A Mater* **2018**, *6* (19), 9064–9073. https://doi.org/10.1039/c8ta01570h.

(24) Ma, M.; Wang, H.; Xiong, L.; Huang, S.; Li, X.; Du, X. Self-Assembled Homogeneous SiOC@C/Graphene with Three-Dimensional Lamellar Structure Enabling Improved Capacity and Rate Performances for Lithium Ion Storage. *Carbon N Y* **2022**, *186*, 273–281. https://doi.org/10.1016/j.carbon.2021.10.026.

(25) Kim, M. S.; Bhattacharjya, D.; Fang, B.; Yang, D. S.; Bae, T. S.; Yu, J. S. Morphology-Dependent Li Storage Performance of Ordered Mesoporous Carbon as Anode Material. *Langmuir* **2013**, *29* (22), 6754–6761. https://doi.org/10.1021/la401150t.

(26) Rodier, B.; de Leon, A.; Hemmingsen, C.; Pentzer, E. Controlling Oil-in-Oil Pickering-Type Emulsions Using 2D Materials as Surfactant. *ACS Macro Lett* **2017**, *6* (11), 1201–1206. https://doi.org/10.1021/acsmacrolett.7b00648.

(27) Vassaux, S.; Savary, G.; Le, L.; Grisel, M. On the Key Role of Process Parameters to Control Stability and Properties of Pickering Emulsions Stabilized by Montmorillonite. *Colloids and Surfaces A* **2019**, *583*, 123952. https://doi.org/10.1016/j.colsurfa.2019.123952.

(28) Gonzalez Ortiz, D.; Pochat-Bohatier, C.; Cambedouzou, J.; Bechelany, M.; Miele, P. Exfoliation of Hexagonal Boron Nitride (h-BN) in Liquide Phase by Ion Intercalation. *Nanomaterials* **2018**, *8* (9), 716. https://doi.org/10.3390/nano8090716.

(29) Cao, H.; Escamilla, M.; Arole, K. D.; Holta, D.; Lutkenhaus, J. L.; Radovic, M.; Green, M. J.; Pentzer, E. B. Flocculation of MXenes and Their Use as 2D Particle Surfactants for Capsule Formation. *Langmuir* **2021**, *37* (8), 2649–2657. https://doi.org/10.1021/acs.langmuir.0c03244.

(30) Rodier, B.; De Leon, A.; Hemmingsen, C.; Pentzer, E. Controlling Oil-in-Oil Pickering-Type Emulsions Using 2D Materials as Surfactant. *ACS Macro Lett* **2017**, *6* (11), 1201–1206. https://doi.org/10.1021/acsmacrolett.7b00648.

(31) Sun, Z.; Feng, T.; Russell, T. P. Assembly of Graphene Oxide at Water/Oil Interfaces: Tessellated Nanotiles. *Langmuir* **2013**, *29* (44), 13407–13413. https://doi.org/10.1021/la402436w.

(32) Marcano, D. C.; Kosynkin, D. V.; Berlin, J. M.; Sinitskii, A.; Sun, Z.; Slesarev, A.; Alemany, L. B.; Lu, W.; Tour, J. M. Improved Synthesis of Graphene Oxide. *ACS Nano* **2010**, *4* (8), 4806–4814. https://doi.org/10.1021/nn1006368.

(33) Dey, S.; Mujib, S. Bin; Singh, G. Enhanced Li-Ion Rate Capability and Stable Efficiency Enabled by MoSe2 Nanosheets in Polymer-Derived Silicon Oxycarbide Fiber Electrodes. *Nanomaterials* **2022**, *12* (553). https://doi.org/10.3390/nano12030553.

(34) Narayanan, S. R.; Shen, D. H.; Surampudi, S.; Attia, A. I.; Halpert, G. Electrochemical Impedance Spectroscopy of Lithium-Titanium Disulfide Rechargeable Cells. *J Electrochem Soc* **1993**, *140* (7). https://doi.org/10.1149/1.2220729.

(35) Magar, H. S.; Hassan, R. Y. A.; Mulchandani, A. Electrochemical Impedance Spectroscopy (Eis): Principles, Construction, and Biosensing Applications. *Sensors*. 2021. https://doi.org/10.3390/s21196578.

(36) Jang, J.; Pham, V. H.; Rajagopalan, B.; Hur, S. H.; Chung, J. S. Effects of the Alkylamine Functionalization of Graphene Oxide on the Properties of Polystyrene Nanocomposites. *Nanoscale Res Lett* **2014**, *9* (1), 265. https://doi.org/https://doi.org/10.1186/1556-276X-9-265.

(37) Shanmugharaj, A. M.; Yoon, J. H.; Yang, W. J.; Ryu, S. H. Synthesis , Characterization , and Surface Wettability Properties of Amine Functionalized Graphene Oxide Films with Varying Amine Chain Lengths. *J Colloid Interface Sci* **2013**, *401*, 148–154. https://doi.org/10.1016/j.jcis.2013.02.054.

(38) Compton, O. C.; Dikin, D. A.; Putz, K. W.; Brinson, L. C.; Nguyen, S. T. Electrically Conductive "Alkylated" Graphene Paper via Chemical Reduction of Amine-Functionalized Graphene Oxide Paper. *Advanced Materials* **2010**, *22* (8), 892–896. https://doi.org/10.1002/adma.200902069.

(39) Ries, L.; Petit, E.; Michel, T.; Diogo, C. C.; Gervais, C.; Salameh, C.; Bechelany, M.; Balme, S.; Miele, P.; Onofrio, N.; Voiry, D. Enhanced Sieving from Exfoliated MoS2 Membranes via Covalent Functionalization. *Nat Mater* **2019**, *18* (10), 1112–1117. https://doi.org/10.1038/s41563-019-0464-7.

(40) Rodier, B. J.; De Leon, A.; Hemmingsen, C.; Pentzer, E. Polymerizations in Oil-in-Oil Emulsions Using 2D Nanoparticle Surfactants. *Polym Chem* **2018**, *9* (13), 1547–1550. https://doi.org/10.1039/c7py01819c.

(41) Valkama, E.; Haluska, O.; Lehto, V. P.; Korhonen, O.; Pajula, K. Production and Stability of Amorphous Solid Dispersions Produced by a Freeze-Drying Method from DMSO. *Int J Pharm* **2021**, *606*, 120902. https://doi.org/10.1016/j.ijpharm.2021.120902.

(42) He, Y.; Wu, F.; Sun, X.; Li, R.; Guo, Y. Factors That Affect Pickering Emulsions Stabilized by Graphene Oxide. *ACS Appl. Mater. Interfaces* **2013**, *5* (11), 4843–4855. https://doi.org/10.1021/am400582n.

(43) Destribats, M.; Faure, B.; Birot, M.; Babot, O.; Schmitt, V.; Backov, R. Tailored Silica Macrocellular Foams: Combining Limited Coalescence-Based Pickering Emulsion and Sol-Gel Process. *Adv Funct Mater* **2012**, *22* (12), 2642–2654. https://doi.org/10.1002/adfm.201102564.

(44) Guo, L.; Ma, Q.; Hu, Z.; Xu, C. High-Temperature Evolution Behavior of MK Silicon Resin Derived SiOC Ceramics under Different Environments. *Ceram Int* **2021**, *47* (15), 21815–21821. https://doi.org/10.1016/j.ceramint.2021.04.198.

(45) Kaur, S.; Mônego, G.; Rezwan, K.; Wilhelm, M. Synthesis of Porous Ni/SiC(O)-Based Nanocomposites: Effect of Nickel Acetylacetonate and Poly(Ethylene Glycol) Methacrylate Modificatidion on Specific Surface Area and Porosity. *Adv Eng Mater* **2020**, *22* (4). https://doi.org/10.1002/adem.201901036.

(46) Adam, M.; Wilhelm, M.; Grathwohl, G. Polysiloxane Derived Hybrid Ceramics with Nanodispersed Pt. *Microporous and Mesoporous Materials* **2012**, *151*, 195–200. https://doi.org/10.1016/j.micromeso.2011.10.037.

(47) Shao, G.; Hanaor, D. A. H.; Wang, J.; Kober, D.; Li, S.; Wang, X.; Shen, X.; Bekheet, M. F.; Gurlo, A. Polymer-Derived SiOC Integrated with a Graphene Aerogel As a Highly Stable Li-Ion Battery Anode. *ACS Appl Mater Interfaces* **2020**, *12* (41), 46045–46056. https://doi.org/10.1021/acsami.0c12376.

(48) Thommes, M.; Kaneko, K.; Neimark, A. V.; Olivier, J. P.; Rodriguez-Reinoso, F.; Rouquerol, J.; Sing, K. S. W. Physisorption of Gases, with Special Reference to the Evaluation of Surface Area and Pore Size Distribution (IUPAC Technical Report). *Pure and Applied Chemistry* **2015**, *87* (9–10), 1051–1069. https://doi.org/10.1515/pac-2014-1117.

(49) Vu, A.; Qian, Y.; Stein, A. Porous Electrode Materials for Lithium-Ion Batteries-How to Prepare Them and What Makes Them Special. *Adv Energy Mater* **2012**, *2* (9), 1056–1085. https://doi.org/10.1002/aenm.201200320.

(50) Huang, C.; Li, A.; Chao, Z. S. Heterogeneous Catalytic Synthesis of Quinoline Compounds from Aniline and C1-C4 Alcohols over Zeolite-Based Catalysts. *RSC Adv* **2017**, *7* (76), 48275–48285. https://doi.org/10.1039/c7ra08442k.

(51) Liu, X.; Zheng, M. C.; Xie, K. Mechanism of Lithium Storage in Si-O-C Composite Anodes. *J Power Sources* **2011**, *196* (24), 10667–10672. https://doi.org/10.1016/j.jpowsour.2011.08.072.

(52) Gao, F.; Geng, C.; Xiao, N.; Qu, J.; Qiu, J. Hierarchical Porous Carbon Sheets Derived from Biomass Containing an Activation Agent and In-Built Template for Lithium Ion Batteries. *Carbon N Y* **2018**, *139*, 1085–1092. https://doi.org/10.1016/j.carbon.2018.08.010.

(53) McNealy, B. E.; Hertz, J. L. On the Use of the Constant Phase Element to Understand Variation in Grain Boundary Properties. *Solid State Ion* **2014**, *256*, 52–60. https://doi.org/10.1016/j.ssi.2013.12.030.

(54) Messing, M.; Shoa, T.; Habibi, S. EIS from Accelerated and Realistic Battery Aging. In *2021 IEEE Transportation Electrification Conference and Expo, ITEC 2021*; 2021. https://doi.org/10.1109/ITEC51675.2021.9490091.

(55) Pastor-Fernandez, C.; Dhammika Widanage, W.; Marco, J.; Gama-Valdez, M. A.; Chouchelamane, G. H. Identification and Quantification of Ageing Mechanisms in Lithium-Ion Batteries Using the EIS Technique. In *2016 IEEE Transportation Electrification Conference and Expo, ITEC 2016*; 2016. https://doi.org/10.1109/ITEC.2016.7520198.

(56) Dey, S.; Singh, G. Differentiating Cyclability and Kinetics of Na + Ions in Surface-Functionalized and Nanostructured Graphite Using Electrochemical Impedance Spectroscopy. *Batteries* **2023**, *9* (11), 534.